ELSEVIER

Polymer 42 (2001) 4219–4231

polymer

www.elsevier.nl/locate/polymer

Morphology development during phase inversion in isothermal, model experiments: steady simple-shear and quiescent flow fields

N.D.B. Lazo, C.E. Scott*

Department of Materials Science and Engineering, Massachusetts Institute of Technology, MIT room 13-5013, 77 Massachusetts Avenue, Cambridge, MA 02139, USA

Received 14 July 2000; received in revised form 3 October 2000; accepted 10 October 2000

Abstract

The effect of component viscosities on phase inversion was examined under two idealized flow fields: steady simple-shear and quiescent. In both cases, disk samples with a specific initial morphology — major-component pellets in a minor-component matrix — were prepared. For the steady simple-shear flow experiments, the evolution of morphology with strain was determined. The same stages of morphology development were observed in all blends; however, the rate of morphology development decreased with increasing effective viscosity ratio. The quiescent experiments tested whether phase inversion occurred in samples that were annealed for a set time. Blends with lower absolute viscosities phase inverted faster. Lattice-Boltzmann simulations demonstrated a functional dependence of $t_c^* \propto Z^{-0.36}\lambda_0^{-0.73}$ based on the dimensionless time to phase inversion t_c^*, Ohnesorge number Z, and viscosity ratio λ_0. This dependence, when extrapolated to the experimental processing window, agrees with the experimental results and indicates that the *dimensional* time to phase inversion under quiescent conditions depends on $\eta_{\text{minor}}^{0.37}\ \eta_{\text{major}}^{0.27}$. Data from both flow fields indicate that phase inversion occurs when the minor component reaches a critical film thickness. This thickness under steady, simple-shear flow was 0.2–0.3 μm at low strain rates. The results from the two flow fields differ in the driving force behind film thinning: shear deformation of the major component drives film thinning under steady, simple-shear flow; interfacial-tension drives it under quiescent conditions. © 2001 Published by Elsevier Science Ltd.

Keywords: Phase continuity; Coalescence; Lattice Boltzmann

1. Introduction

Many new applications for polymeric materials require a combination of properties that no single commercially available polymer meets. Blending polymers is often a faster and more cost-effective means of achieving the required properties than synthesizing new polymers. A polymer blend's performance critically depends on its morphology. Thus, understanding how the blend's morphology develops during processing and how this depends on the materials' properties will greatly aid process design.

During the compounding of polymer blends in industrial equipment, such as batch mixers and twin-screw extruders, one polymer often softens or melts significantly faster than the other. This work focuses on the situation where the lower-concentration, or minor, component melts before the higher-concentration, or major, component does. In this scenario, the minor component initially forms the matrix in which the major-component pellets are suspended. As the major component heats up, the blend morphology transforms from one where polymer A (the major component) is dispersed in polymer B (the minor component) to the reverse. This transformation, which is illustrated in Fig. 1, is termed a phase inversion.

Phase inversion during compounding was first observed by Shih [1] in 1991 while rubber-toughening polyarylate. Since then, further studies have elucidated how material and process parameters affect the occurrence of phase inversion. The common industrial practice when compounding blends is to simultaneously introduce both polymers in pellet form to the mixing chamber, which is pre-heated to temperatures above the transition temperatures of the polymers. Under these processing conditions and with a 10 wt.% minor-component concentration, phase inversion takes place if the minor component's viscosity is less than about 20% of the major components at a characteristic temperature and strain rate, regardless of the relative values of the components' transition temperatures [2,3]. Furthermore, phase inversion can be induced in blends with unfavorable relative viscosities by adjusting the temperature profile [2] and the addition protocol. Phase inversion is thus expected to occur

* Corresponding author. Tel.: +1-617-258-6113; fax: +1-617-253-6896.
E-mail address: cscott@mit.edu (C.E. Scott).

0032-3861/01/$ - see front matter © 2001 Published by Elsevier Science Ltd.
PII: S0032-3861(00)00779-5

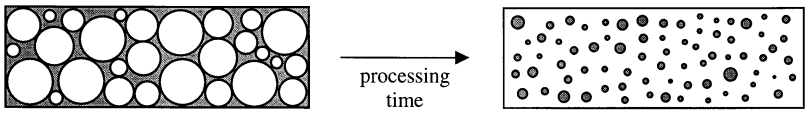

Fig. 1. Schematic illustration of phase inversion during processing.

during, among others, the rubber-toughening of many amorphous polymers and the compounding of polyamide with lower-transition-temperature minor components.

While the above-mentioned works focused on whether phase inversion occurred, others investigated the effect of material and process parameters on how long it takes for phase inversion to occur. Scott and Joung [3] showed that the less viscous the minor component relative to the major one, the longer the processing time required for the blend to phase invert. In addition, they found that the time to phase inversion increased with increasing minor-component concentration, decreasing mixer temperature, and decreasing degree of fill.

1.1. Intermediate morphologies during phase inversion

Phase inversion is in essence a morphological change. Therefore, understanding how the morphology evolves during phase inversion is the key to comprehending the phase inversion mechanism. It will allow identification of the parameters that govern the kinetics of phase inversion, thereby giving process engineers control over the phenomenon. In addition, the intermediate stages of phase inversion may produce unique morphologies with desirable properties.

Shih [4] previously proposed a sequence of four morphological stages during phase inversion:

1. Solid major-component pellets are suspended in a molten minor-component matrix.
2. The surfaces of the pellets heat up and are sheared off the solid core as sheets.
3. The major-component continues to be dispersed in the minor-component. This decreases the minor-component concentration in the melt until it reaches the percolation threshold, the minimum concentration at which a component forms a continuous path across the sample.
4. The blend phase inverts.

Sundararaj et al., [5,6] confirmed the first two steps of this process. In addition, they observed that as the major-component melt concentration increased, it coalesced into irregular domains and encapsulated drops of the minor component in the process. Lee and Han [7] also reported an intermediate co-continuous morphology during Step 4. It is important to note the experimental protocol used in these four works. Specifically, the polymer pellets were simultaneously heated to the processing temperature and deformed by both shear and extensional flows in a batch mixer, and therefore underwent dissipative mix-melting.

The authors have previously reported on phase inversion under isothermal, steady, simple-shear flow [8]. To accomplish this, disk samples were prepared with an initial morphology consisting of major-component pellets in the minor-component matrix. In contrast to the previous works, the samples were first heated up to the processing temperature before they were deformed. The well-defined thermal and flow history enabled identification of morphologies intermediate between the sheets and the final phase-inverted blend. In addition, it was shown that phase inversion can occur in a simple-shear flow field, i.e. elongational flow is not required.

Identifying the mechanism that controls how quickly phase inversion occurs is a key step in mastering the processing–morphology relationship. To date, no criterion has been established to predict the time to phase inversion for any blend under a given set of processing conditions. Other authors [1–4,6,9] have previously suggested that phase inversion occurs at a particular melt composition; i.e. when a sufficient amount of the major component has melted. However, Lazo and Scott's isothermal experiments [8] indicate that under simple-shear flow, and potentially in more complex flow fields, this is not the case. Rather, they support the idea that phase inversion is primarily a coalescence phenomenon. Phase inversion occurs only when the minor-component films are thin enough to allow the major-component domains to spontaneously coalesce, approximately 0.2 μm in that study. Therefore, the rate of film thinning more strongly controls the time to phase inversion than does the rate of melting. Of course, in commercial processes where dissipative mix-melting is important, film thinning and melting are closely coupled. However, based partly on these results, Ratnagiri [10] successfully used a strain-based criterion to explain the effect of scaling up from a small to a large batch mixer on the time to phase inversion. His approach assumed that particular blend phase inverted when the dispersed major-component domains were deformed to a critical strain. There is currently insufficient data, however, to prove a morphology-based criterion, much less predict its value for any given blend.

This work seeks to help fill this gap in the knowledge base. To accomplish this, phase inversion under two idealized flow fields — steady simple-shear and quiescent — is investigated. Two fundamental questions concern the steady, simple-shear flow field. First, what parameters affect the rate of film thinning and other morphology

Table 1
Rheological properties of materials used

Polymer	Supplier	Commercial name	Viscosity at 0.5 s^{-1} and 180°C (Pa s)	Zero-shear viscosity at 180°C (Pa s)
PS	Amoco	1-R100-W0	57 000	140 000
HDPE	Dow chemical	HDPE 04452N	4000	10 000
LDPE	Eastman chemical	Epolene C-14	8300	13 000
LDPE	Eastman chemical	Epolene C-17	1100	1500
LDPE	Eastman chemical	Epolene C-13	–	70
PCL	Union carbide	Tone 787	4800	4900
PCL	Union carbide	Tone 767e	510	510

development? This study focuses on the effect of component rheologies because the viscosity ratio has been shown to strongly affect the time to phase inversion [3]. Second, what is the critical film thickness for spontaneous coalescence?

Two other questions deal with phase inversion in a quiescent flow field. As mentioned above, phase inversion is, at its most basic level, simply the coalescence of the major-component domains. Uncompatibilized-blend morphologies are known to coarsen when annealed above their transition temperatures [11–13]. Therefore, can phase inversion occur under quiescent conditions? The sequence of events leading to coalescence includes a film-thinning step [14], just as in phase inversion. Fortelny's theory [14] predicts that the rate of film thinning depends on the components' viscosities. What, therefore, is the effect of the materials' rheological properties on the time to phase inversion? Finally, can a criterion for phase inversion be derived from the results of both flow fields?

In summary, this work explores the effect of the components' rheological properties on phase inversion under two idealized flow fields: steady simple-shear and quiescent. In both cases, disk samples were prepared with a specific initial morphology: major-component pellets suspended in a minor-component matrix. The morphology as a function of strain was determined for the steady shear-flow experiments. The quiescent experiments investigated whether phase inversion occurred after the samples were annealed for a set time.

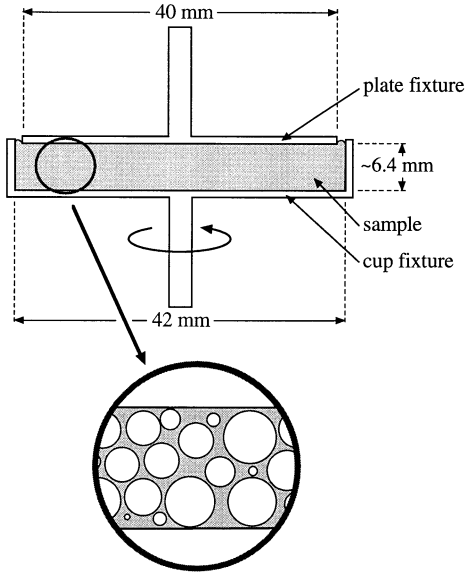

Fig. 2. Schematic diagram of the cup-and-plate fixture and the initial sample morphology consisting of three interpenetrating layers of major-component pellets in a minor-component matrix.

2. Experimental method

The model blends investigated were polystyrene/polyethylene and polyethylene/polycaprolactone (major/minor). The minor-component concentration was 16 vol% in all cases. The sole polystyrene (PS) was Amoco's 1-R100-W0. One polyethylene (PE) was HDPE 04452N, a high-density polyethylene from the Dow Chemical Company. The remaining polyethylenes were low-density polyethylenes obtained from the Epolene® line of the Eastman Chemical Company. The two polycaprolactones were from Union Carbide Corporation's Tone® line of polymers. Table 1 summarizes the polymers used, including their sources and commercial designations. It also lists the viscosities at 0.5 s^{-1} and at the zero-shear limit for the polymers employed in each flow field. The melt viscosities were measured using the 25- or 40-mm parallel-disk fixture in a Rheometric Scientific ARES strain rheometer.

2.1. Sample preparation

The sample disks, which measured roughly 40.2 × 6.5 mm^2, were carefully prepared by compression molding. The initial morphology consisted of three interpenetrating layers of major-component pellets in a minor-component matrix, as shown in Fig. 2. To create this morphology, the minor component was first pressed into four paper-thin sheets. One sheet was then used to line the bottom of the heated mold and a layer of major-component pellets was spread onto it. Another minor-component sheet was laid on top of this and heated until it softened. The sheet was then manipulated with tweezers to keep the pellets separated. The layering process was repeated until the three pellet layers were formed. The pressure on the mold was gradually increased to 250 bar and held for 5 min. The mold was air-cooled under a weight of 5 kg for 15 min before the sample was unloaded. This disk-molding procedure was fine-tuned for each blend to produce the correct blend composition and eliminate bubbles. Such adjustments comprise altering the mold temperature and changing the pre-molding component concentrations. This technique will produce the target morphology only if the minor component is considerably less viscous than the major component at the molding temperature.

2.2. Experimental technique and morphological characterization

The cup-and-plate fixture shown in Fig. 2 was installed in a Rheometrics ARES strain rheometer and used for these

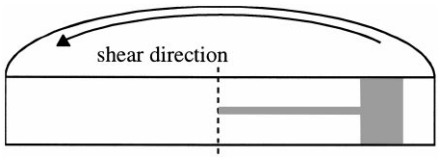

Fig. 3. Schematic diagram of the fracture surface relative to the shear direction. The grey region was examined at 200× magnification.

experiments. After the sample was loaded at room temperature, the chamber was gradually heated up to 180°C over 15–30 min and allowed to equilibrate for 15 min. The plate was lowered such that the sample appears as illustrated in Fig. 2: in full contact with, but not overflowing on top of, the plate. Because setting the plate position required the chamber to be opened, the apparatus was again allowed to equilibrate at 180°C for 30 min.

The experimental procedure for the steady-shear and quiescent experiments is the same until sample loading, but differ thereafter. In the steady-shear experiments, a strain rate of 0.5 s^{-1} at the rim of the plate was applied. Samples for each blend were sheared to total strains of 100, 500, 1000, and 4000 at the rim. After each run, the fixture and samples were quickly quenched in liquid nitrogen for 10 min. The fixture was reheated to the lowest possible temperature (65–135°C) that allowed the sample to be removed. The samples were fractured perpendicular to the shear direction at cryogenic temperatures. They were subsequently exposed to dichloromethane in a Soxhlet extraction apparatus to selectively dissolve the polystyrene or polycaprolactone. The extracted fracture surfaces were examined using an ElectroScan E3 environmental scanning electron microscope. The examined regions are shown in grey in Fig. 3.

Because of the sidewall in the cup fixture, the velocity profile deviates considerably from linearity close to the wall. Simulation of the resulting flow field in a homogeneous fluid indicated that the strain rate at the fixture surface differed by 10% from the average at a radius of 14 mm and 50% at 18 mm [8]. To account for the strain rate inhomogeneity, data beyond 18 mm were excluded from the following analysis. Furthermore, in the region where the strain rate depends on axial position, i.e. at radial distances of 14–18 mm, the entire fracture surface was examined. The morphology was independent of the strain rate for the strain rates used in this study [8].

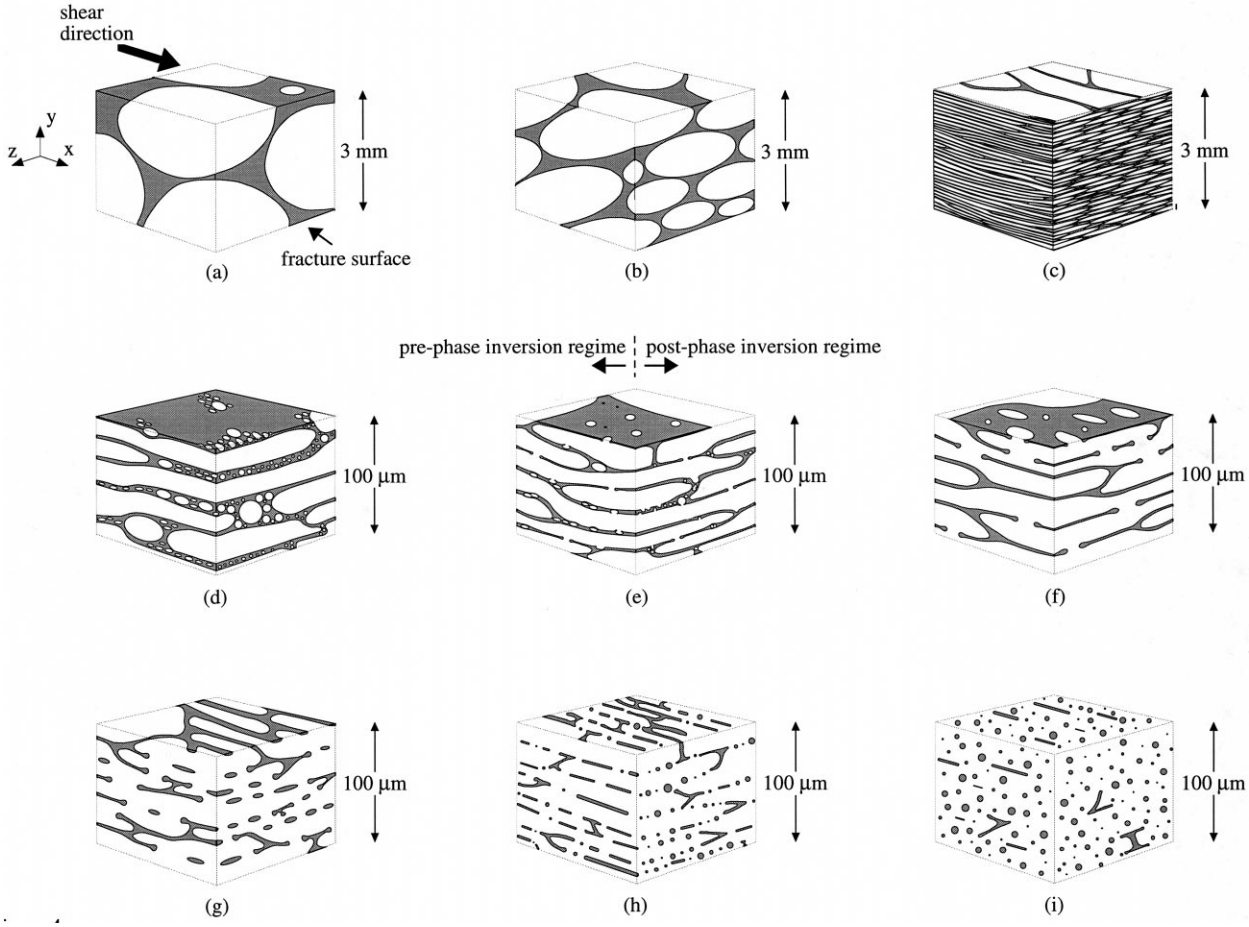

Fig. 4. Schematic illustration of morphology development during phase inversion under steady simple-shear flow. There is a change of scale between (c) and (d). The short bar beside the 3-mm scale bar in (c) is the 100-μm scale bar.

Table 2
Stages of morphology development used in morphological analysis

Stage	Major-phase morphology	Minor-phase morphology	Corresponding figure	Regime relative to phase inversion
1	Pellets	Continuous	Fig. 5a	Pre
2	Sheets	Continuous	Fig. 5c	Pre
3	Ribbons and drops	Continuous	Fig. 5d	Pre
4	Coalescence onset	Continuous sheet with holes	Fig. 5e	Onset
5	Continuous	Continuous strand network	Fig. 5g	Post
6	Continuous	Fibers and drops	Fig. 5i	Post

In the quiescent experiments, the samples were held at 180°C for an additional 2000 s, or approximately 33 min, which is equivalent to the 1000-strain run time. The samples were quickly quenched in liquid nitrogen and removed from the fixture, as described above. They were examined by eye and by stereo-optical microscopy to determine if phase inversion had occurred.

3. Results and discussion

3.1. Steady-shear experiments

All the blends exhibited the same sequence of morphologies described previously [8] and illustrated in Fig. 4. Specifically, the major component starts out as pellets at zero strain and stretches into sheets when strain is applied. Some of the major component breaks off to form ribbons and drops. Meanwhile, the increasing major-component domain deformation causes the minor-component films separating those domains to progressively reduce in thickness. When the films become sufficiently thin, 0.2–0.3 μm in these blends, holes form in the films and the major-component domains begin to coalesce. The holes lengthen preferentially in the velocity direction forming a co-continuous strand network. Eventually, fibers break off from the minor-component strand network and the fibers break up into drops.

3.2. Morphological measure

Precise quantification of the changes described above is a major challenge for morphological analysis. Blends with

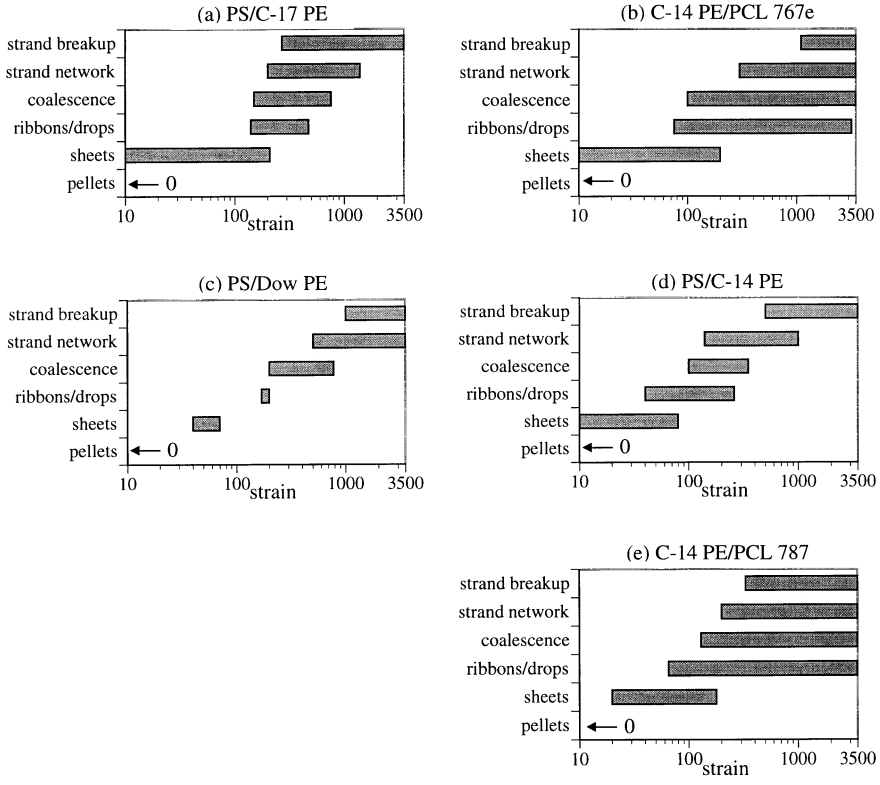

Fig. 5. Summary of the strain ranges at which the morphological stages are observed for each blend. In decreasing order of major-component to minor-component viscosity: (a) PS/C-17 PE; (b) C-14 PE/PCL 767; (c) PS/HDPE; (d) PS/C-14 PE; and (e) C-14 PE/PCL 787.

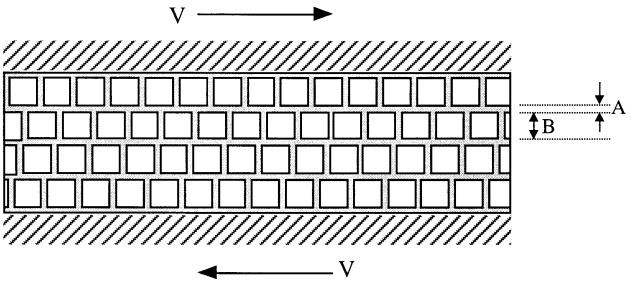

Fig. 6. Two-dimensional model morphology, consisting of layers of square major-component domains in a minor-component matrix, used for determining the effective matrix viscosity.

unchanging continuous and dispersed phases are easily described by the evolution of the drop-size distribution. However, the morphology development during phase inversion is extremely complex. The pertinent data include the size reduction and shape changes of the major component prior to phase inversion, the size reduction of the minor component after phase inversion, and the extent to which the major component has coalesced. No single known morphological measure captures all these changes. Therefore, the morphology was instead characterized by the six distinct stages of morphology development listed in Table 2. This is possible because all the blends exhibited the same sequence of morphologies.

The strain ranges at which these morphological stages were observed in the various blends are illustrated in Fig. 5. The data here represent the dominant morphologies at a particular strain. Because there are local variations in the initial minor-component film thickness, there is often a range of morphologies at a given strain. There are two notable differences among the blends. First, the minimum strain at which each stage appears varies considerably between blends. Second, stages 2 and 3 persist to higher strains in the PE/PCL blends.

All further analysis was based on the minimum strain at which each morphological stage was observed. Because of the nature of the selective dissolution technique, it is easier to detect the minimum strain at which a morphology occurs than the maximum one. In particular, the relative persistence of stages 2 and 3 in the PE/PCL blends may be an artifact of this technique.

3.3. Effective viscosity-ratio calculation

The viscosity ratio is known to be a key parameter influencing drop deformation and breakup under simple-shear flow [15,16]. In the extensive literature covering this idealized flow field, blends have generally consisted of a single drop in an essentially infinite matrix. The viscosity ratio here is easily defined as $\lambda = \eta_d/\eta_c$, where η_d and η_c are the dispersed- and continuous-phase viscosities, respectively.

Previous works have simply used $\eta_{minor}/\eta_{major}$ to characterize their blends even when their systems differ remarkably from the infinitely dilute one. However, there are two critical differences between this simple morphology and the focus of the present work which require that greater care be taken in defining the viscosity ratio. First, there is an exchange of the dispersed and continuous phases before and after phase inversion. In the pre-phase inversion regime, stages 1–4 in Table 2, the major component is considered the dispersed phase. Conversely, the minor component is deemed the dispersed phase in the post-phase inversion regime, stages 4–6.

Second, the pre-phase-inversion dispersed-domain concentration of 84% by volume vastly differs from the infinitely dilute system. Thus, it is more appropriate to treat each dispersed domain in the present blend as a domain within a uniform matrix, where the matrix has the rheology of the blend, termed the effective matrix viscosity. The large concentration of the dispersed phase generally yields an effective matrix viscosity that substantially deviates from that of the pure matrix.

Fig. 6 illustrates a two-dimensional morphology that closely approximates the one at the beginning of the experiment. Here, the minor-component films separating the square major-component domains are assumed to be the same thickness in the *x*- and *y*-directions. Viewing this scenario as a series structure of A and B layers, where the B layer is a parallel structure of the major and minor components, the effective matrix viscosity in the pre-phase inversion regime is estimated as:

$$\eta_{eff} = \eta_{minor} \frac{\phi_1 + \lambda_0 \phi_2}{\phi_1^2 + \lambda_0 \phi_1 \phi_2 + \phi_2} \tag{1}$$

and the effective viscosity ratio is:

$$\lambda_{eff} = \lambda_0 \left[\frac{\phi_1^2 + \lambda_0 \phi_1 \phi_2 + \phi_2}{\phi_1 + \lambda_0 \phi_2} \right] \tag{2}$$

where $\lambda_0 = \eta_{major}/\eta_{minor}$, $\phi_1 = 1 - \sqrt{\phi_{major}}$, $\phi_2 = \sqrt{\phi_{major}}$, and ϕ_{major} is the volume fraction of the major component. The complete derivation is in Appendix A. Note that the effect of the interfacial-tension was neglected here, which is acceptable to a first approximation because of the large size of the domains [17]. A similar derivation for the effective viscosity ratio in the post-phase inversion regime was accomplished.

To validate this approach to calculating the effective viscosity ratio, the drop deformation results are compared with the literature. Rumscheidt and Mason [18] report that drops in a blend with a viscosity ratio of 6 reached an equilibrium deformation at an aspect ratio of 2. Combining the data in Table 3 and Fig. 5 shows that a straightforward viscosity-ratio calculation of $\eta_{major}/\eta_{minor}$ for the pre-phase inversion regime results in a pellet-to-sheet deformation of the dispersed domain at larger viscosity ratios. In contrast, the effective viscosity ratios are actually lower than 6, which can explain the much higher aspect ratios of the sheet morphology. Because the effective viscosity-ratio calculation makes the blends' results consistent with Rumscheidt

Table 3
Summary of viscosity ratio calculations for the pre-phase inversion regime: unadjusted viscosity ratio and effective viscosity ratio based on the morphology in Fig. 7

Blend	$\lambda_0 = \frac{\eta_{major}}{\eta_{minor}}$	λ_{eff}
PS/Dow PE	12	2.0
PS/C-14 PE	6.9	1.6
PS/C-17 PE	52	5.3
C-14 PE/PCL 787	1.7	1.1
C-14 PE/PCL 767e	16	2.4

and Mason's, it is feasible to compare these results using λ_{eff} to those for other infinitely dilute systems in simple-shear flow using λ.

3.4. Comparison with previous work

The steady, simple-shear-flow results for the various blends were compared using the stage-based morphological measure and the effective viscosity ratio. In particular, a rate of morphology development was determined. For each blend, a line was fit to the minimum-strain data for both pre- and post-phase inversion regimes. The slope of each line is the rate of morphology development, or dM/d(strain).

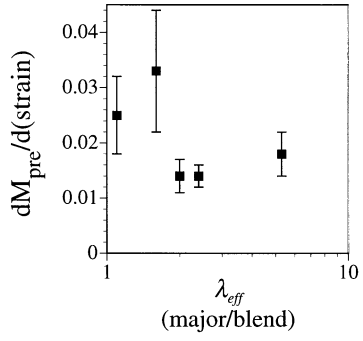

(a)

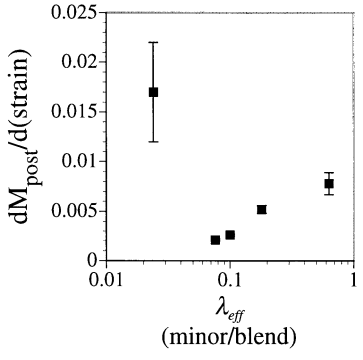

(b)

Fig. 7. Rate of morphology development as a function of effective viscosity ratio for the (a) pre- and (b) post-phase inversion regimes. The error bars are smaller than the data points for three cases in (b).

The results for both regimes are plotted as a function of effective viscosity ratio in Fig. 7.

A preliminary analysis of Fig. 7 indicates that the rate of morphology development is faster for lower-viscosity-ratio blends in both the pre- and post-phase inversion regimes. To compare these results with the available literature, it is useful to define the important mechanisms for drop deformation and breakup based on the experimental conditions. Analyses of these phenomena generally use the viscosity ratio, λ, and the capillary number, Ca, to characterize the experimental conditions [15,16,19,20]. The latter is a relative measure of the shear forces that cause drop deformation against the interfacial-tension that hinders it. Ca is defined as $\eta_c \dot{\gamma} D/\sigma$, where η_c is the matrix viscosity, $\dot{\gamma}$ the strain rate, D the drop diameter, and σ the interfacial-tension. Below the critical Ca, Ca_c, the drop reaches a stable deformation in the flow; above it, the drop breaks up.

In the regime where the major component is dispersed in the present experiments, the relevant data from prior literature concern the unsteady-state drop deformation as a function of λ and Ca for $Ca > 10$. As the minor-component film thickness approaches 0.2–0.3 μm, the critical information is that dealing with spontaneous coalescence and its dependence on λ and Ca.

Finally, when the minor component is dispersed, details of the unsteady-state drop deformation as a function of λ and Ca are again crucial, but this time for $1 \leq Ca \leq 10$. In addition, the minor-component strand network may break up via capillary instabilities. Hence, the dependence of capillary breakup on λ and Ca is also of interest. The three mechanisms, then, whose dependence on λ and Ca under steady shear flow are of particular importance are:

1. Unsteady-state drop deformation;
2. Spontaneous coalescence; and
3. Capillary breakup.

3.4.1. Unsteady-state drop deformation

There is a considerable body of work focusing on drop deformation in steady shear-flow. However, most of it is not directly applicable here because those works consider steady-state drop deformation at capillary numbers below the critical value. The authors know of only two works [16,21] that investigate unsteady-state drop deformation and their results, which are discussed below, seem to contradict each other. Of the two, Marks' data [21] more closely approaches what is needed in the present work. He separated drop deformation from breakup by tracking the evolution of the minor axis with time. In contrast, Grace [16] reported the reduced burst time ($t_b^* = t_b \sigma/\eta_c D$, where t_b is the time required for the drop to burst), which is affected by both drop deformation and breakup. This difference may explain the apparent discrepancy in their outcome. The experimental spaces that they explored overlapped: Marks' experiments had $0.0087 \leq \lambda \leq 1.4$ and $1 \leq Ca/Ca_c \leq 6$;

Grace's had $10^{-4} \leq \lambda \leq 0.1$ and $1 \leq Ca/Ca_c \leq 13$. Ca/Ca_c is termed the reduced capillary number.)

Marks found that the minor-axis evolution follows that predicted by homogeneous deformation for reduced capillary numbers greater than 2. In addition, nominal numbers representing the shape and magnitude of the deformation vs. time curve are reported to be independent of λ. Based on this, the morphology as a function of strain and the rate of morphology development in the present study should be independent of λ_{eff}. Results for the pre-phase inversion regime clearly disagree with this, as shown in Fig. 7a. (So do the results for the post-phase inversion regime. Capillary breakup must be accounted for in this regime, however, so this will be discussed later). The rate of morphology development was higher by a factor of 2 for lower viscosity ratios. There are a number of possible explanations for this. First, Marks did not present the viscosity-ratio data; it is possible that the variance in the present results is comparable to his. Second, the viscosity-ratio range in this regime is different from that studied by Marks. Third, interfacial slip may be occurring in the present blends, but not in Marks's. Interfacial slip hinders the homogeneous deformation of the blend. Using the effective matrix viscosity, the shear stresses in the present blends are all greater than 10^3 Pa. These values approach or exceed the critical shear stress for slip of 2×10^3 Pa reported by Zhao and Macosko [22]. In contrast, the shear stresses in Marks's blends are less than 100 Pa. It was also previously shown that the major component does not deform homogeneously in the pre-phase inversion regime for the PS/Dow HDPE blend [8].

In contrast to Marks, Grace reported a significant, though less-than-proportional, decrease of the reduced burst time with reduced capillary number. In addition, the drop deformation at burst increased with reduced capillary number. These two results, together, indicate that the rate of morphology development increases with capillary number. Marks pointed out, however, that both the reduced burst time and the reduced capillary number are, respectively, directly and inversely proportional to $\sigma/\eta_c D$. This dependence may overwhelm any relationship between t_b^* and the reduced capillary number. Regardless of the effect of the capillary number, however, Grace found that the reduced burst time increased, and the drop deformation decreased, with λ for the entire capillary number range. This predicts that the rate of morphology development decreases with λ_{eff}, which agrees with the results of the pre-phase inversion regime in the present study.

3.4.2. Spontaneous coalescence

When Elmendorp and Van der Vegt [23] examined drop coalescence under simple-shear flow, they calculated the probability that the film separating two colliding drops would thin down to a critical thickness, h_c, before the drops separated in the flow. At this critical thickness, Van der Waals forces would spontaneously rupture the film and the drops would coalesce. Because of the high dispersed-phase concentration in the present work, the deformation of the dispersed phase itself is expected to drive the film reduction to the critical thickness. The impact of λ and Ca on this phenomenon was discussed in the previous section. What bears investigation in this section, therefore, is the dependence of the critical thickness on λ. Its dependence on Ca has not been reported. According to Vrij [24], the critical thickness can be calculated as:

$$h_c \approx 0.222\left(\frac{c^2 A}{6\sigma}\right)^{1/4} \tag{3}$$

where c is the radius of the contact area between the two coalescing domains, A the Hamaker constant, and σ the interfacial-tension. A larger h_c increases the probability of coalescence and reduces the time to phase inversion. To a first approximation, A and σ are independent of λ. The extent of deformation, which has been shown here to depend on λ, is expected to be the main factor determining c. The results here indicate that dispersed domains in blends with lower effective viscosity ratios in the pre-phase inversion regime deform faster and therefore have a larger contact area at a given strain. It would seem likely then that the lower-viscosity-ratio blends have a larger h_c, thereby enhancing any differences in the rate of morphology development among the blends. However, in the present work, h_c was 0.2–0.3 μm across all the blends, indicating that it is not strongly affected by λ. This value is much larger than the critical film thickness of 0.02–0.05 μm predicted by Eq. (3), but agrees with that reported by Grizzuti and Bifulco [25] of 0.2–0.26 μm in polydimethylsiloxane/polyisobutylene blends at strain rates less than 1 s^{-1}.

On a related note, Scott and Joung [3] reported that decreasing the minor-component viscosity increased the time required for a blend to phase invert in a batch mixer. This concurs with the present results where higher λ_{eff} decreased the rate of morphology development prior to phase inversion and did not affect the critical film thickness for coalescence.

3.4.3. Capillary breakup

Most works on capillary breakup are grounded on Tomotika's theory [26] for thread breakup in a quiescent viscous medium. These results may thus have limited applicability to this study because of the difference in flow fields. However, Patlazhan and Lindt [27] point out that for small shear rates and for drops that are sufficiently stretched, the quiescent assumption is valid and Tomotika's predictions apply. Those two conditions certainly apply in the present study: $\dot{\gamma} \leq 0.5\ s^{-1}$ and the domains that are breaking up are highly stretched fibrillar networks. The works on capillary breakup have confirmed experimentally and theoretically that the normalized breakup time increases with increasing λ [21,26–28]. The rate of morphology development is expected to vary inversely with the normalized breakup time and therefore decrease with λ_{eff}.

Table 4
Results summary of the quiescent phase-inversion experiments

System (major/minor)	Major-component zero-shear viscosity (Pa s)	Minor-component zero-shear viscosity (Pa s)	λ_0	Phase inversion after 2000 s at zero strain
PS/PE-10000	140 000	10 000	14	No
PE-13000/PCL-4900	13 000	4 900	2.7	No
PE-13000/PCL-510	13 000	510	25	No
PE-1500/PCL-4900	1500	4900	0.31	Yes (starting)
PE-1500/PCL-510	1500	510	2.9	Yes
PE-70/PCL-4900	70	4900	0.014	Yes (starting)
PE-70/PCL-510	70	510	0.14	Yes

The post-phase inversion blends fall in the viscosity-ratio range studied by Marks [21] where he found that drops at reduced capillary numbers greater than two exhibited homogeneous deformation regardless of the viscosity ratio. The lower capillary breakup time of the lowest-viscosity-ratio blend, however, explains why the rate of morphology development is roughly four times larger in this blend than in the others. The post-phase inversion regime data are also consistent with Grace's results [16].

In summary, analysis of the steady, simple-shear-flow results draws on the expertise in drop deformation in infinitely dilute systems. The calculation of an effective viscosity ratio enabled this comparison. The results indicate that the rate of morphology development decreases with increasing λ_{eff} in both pre-and post-phase inversion regimes. These experimental findings are consistent with most of the literature. In addition, major-component domains coalesced, and therefore phase inversion began, only when the minor component reached a critical film thickness of 0.2–0.3 μm. This critical value did not depend on materials properties in the present study. It was the shear deformation of the major component that drove film thinning in these experiments.

3.5. Quiescent experiments

The results for the quiescent-coalescence experiments are summarized in Table 4. Also included in the table are the components' zero-shear viscosities and the corresponding viscosity ratios. The table is sorted primarily by the major-component viscosity and secondarily by that of the minor-component. Unlike the steady-shear-flow experiments, the experimental results seem to indicate that phase inversion under quiescent conditions is not controlled by the viscosity ratio. Although the blends with the highest viscosity ratios did not phase invert after 2000 s and those with the lowest viscosity ratios did, the trend does not continue to the rest of the blends. In particular, the PE-1500/PCL-510 blend went farther along the phase inversion process than two blends (PE-13000/PCL-4900 and PE-1500/PCL-4900) with lower viscosity ratios. Rather, the results indicate that the kinetics of phase inversion are more strongly dependent on the absolute viscosities of the components. To better understand these results, it is useful to compare these data with the available theoretical models.

3.6. Previous work

The coalescence of two drops generally occurs by the following sequence of events [14]:

1. Approach of the two drops;
2. Drainage of the film separating the drops;
3. Film rupture; and
4. Evolution of the neck connecting the drops.

Theoretical treatments have assumed various driving forces for quiescent coalescence. Smoluchowski [29–31] (as cited in Ref. [14]) analyzed the case where Brownian motion induces coalescence. He predicted the increase in drop size with time when drop approach is the rate-limiting step, an assumption that holds only for low drop concentrations. For drop concentrations greater than 10%, Fortelny and Zivny [14] postulated that film drainage is the rate-limiting step. They considered gravity and Van der Waals forces, as well as Brownian motion, as driving forces for coalescence. They then derived the time-dependence of the film thickness for different interfacial mobilities, which is influenced by the viscosity ratio. Only the interfacial-mobility contribution depends on the component viscosities. The rate of film drainage was inversely related to either the matrix or drop viscosity; which viscosity depended on the interfacial-mobility.

Coalescence times for the present work were calculated using Fortelny and Zivny's theory but the theory failed to correctly rank the blends. In addition, this theory does not account for what is expected to be the strongest driving force here — the interfacial-tension. Because of their high concentration, the dispersed-phase domains are deformed from the spherical shape that minimizes the interfacial area. The domains will try to achieve a spherical shape and, in so doing, induce film drainage and coalescence.

3.7. Simulation

Numerical simulation of phase inversion under quiescent conditions was conducted using the lattice-Boltzmann

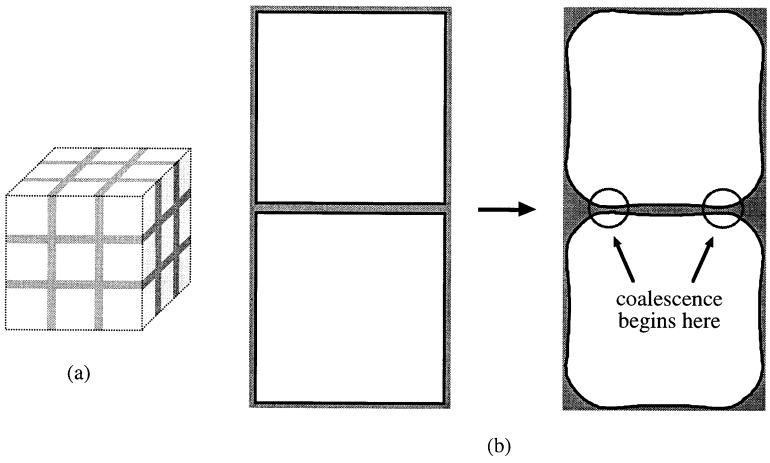

Fig. 8. (a) Model of the initial morphology of the blends, which is used in the lattice-Boltzmann simulations. (b) Cross-section of the model morphology schematically showing quiescent phase inversion driven by interfacial-tension.

method. The details of this approach can be found in the literature [32–36]. Its primary advantage lies in the ease with which it handles movements of the interface, including its deformation, generation, and destruction. The lattice-Boltzmann method used for the simulations shown here is the BGK lattice-Boltzmann method with a single-relaxation parameter and no rest particle. It was written by Suwa [37], who modified a single-relaxation, single-phase, three-dimensional FCHC lattice-Boltzmann code written by van Genabeek [35] into a two-phase, three-dimensional simulation program by faithfully implementing and expressing Rothman's [36] scheme for color separation and formulation of interfacial-tension. This software has successfully simulated several key mechanisms of morphological change in molten polymer blends [38].

The simulation geometry consisted of a periodic array of major-component cubes in a minor-component matrix, as shown in Fig. 8a. Nine independent parameters were identified: the viscosities (η) and densities (ρ) of both fluids, the interfacial-tension σ, the major component's domain size L, the minor component's initial film thickness h, the critical film thickness for coalescence h_c, and the time to phase inversion t_c. The controlling dimensionless groups were determined using the Buckingham Π theorem [39]. Both the experimental and simulation results were analyzed on the basis of these controlling dimensionless numbers. These six independent dimensionless groups are listed in Table 5. The first five are the input variables, and their experimental and computational values are included in Table 5; the last, t_c^*, is the output result. Most of the dimensionless groups are self-explanatory. The Ohnesorge number is the ratio of the viscous force resisting film thinning to the interfacial-tension and inertial forces

Table 5
Dimensionless groups used for the quiescent phase inversion simulations

Dimensionless group	Formula	Experimental values	Computational values
Viscosity ratio	$\lambda_0 = \frac{\eta_{major}}{\eta_{minor}}$	0.014–27	0.3–3.3
Density ratio	$\frac{\rho_{major}}{\rho_{minor}}$	0.82–1.2	1
Ohnesorge number	$Z = \frac{\eta_{minor}}{\sqrt{\sigma \rho_{minor} h}}$	23 000–220 000	0.05–0.5
Dimensionless film thickness (or volume fraction)	$h^* = \frac{h}{L}$	0.056	0.087–0.091
Dimensionless critical film thickness	$h_c^* = \frac{h_c}{L}$	0.00067	0.030–0.043
Dimensionless time	$t_c^* = \frac{\sigma t_c}{\eta_{major}(h - h_c)}$	Result	Result

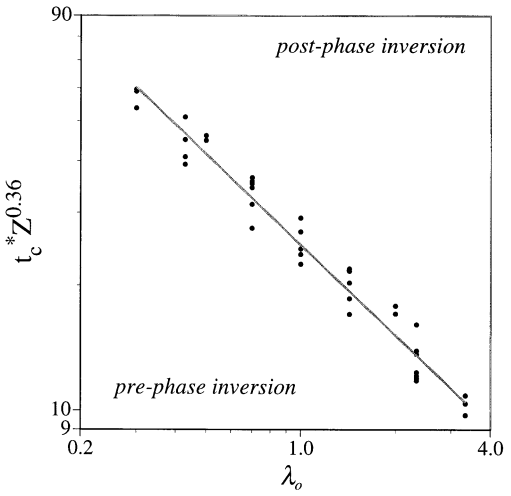

Fig. 9. Summary of the lattice-Boltzmann simulation results. The data indicate the onset of phase inversion. The slope of the master curve is −0.73.

propagating film thinning. The effective matrix viscosity, and therefore the effective viscosity ratio, are not used here because the current set of dimensionless parameters allows for simpler interpretation of the results.

The Buckingham Π theorem states that t_c^* can be expressed as a function of the other five dimensionless variables. However, some variables influence the time to phase inversion more than others. Three parameters — the density ratio, dimensionless film thickness, and dimensionless critical film thickness — were eliminated from the parameter space of investigation for the reasons outlined below.

The density difference between the two components is important only in gravity-driven, rather than interfacial-tension-driven, film drainage. To determine the significance of the density ratio then, one must consider the relative values of the gravitational and the interfacial-tension forces. This is represented by the Bond number, $g\Delta\rho R_u/3\sigma$, where g is the acceleration of gravity, $\Delta\rho$ the density difference, R_u the undeformed-drop radius, and R_c the minimum radius of curvature of the interface. The Bond number attains values of 0.1–0.4 in the present systems, indicating that gravity is less important than interfacial-tension for the blends studied. Thus, simulations were limited to a density ratio of one.

The dimensionless film thickness, h^*, is related to the minor-component volume fraction and $(h^* - h_c^*)$ determines the amount of material that must be locally drained for coalescence. One would expect that t_c^* depends on the volume fraction. In fact, if h^* is sufficiently high, $t_c^* = \infty$. However, it is anticipated that t_c^* becomes independent of h^* below a particular h^*. The Laplace pressure, σ/R_i where R_i is the radius of curvature of the interface, propels the transition of the major component from a cube to a sphere. The driving force is greatest at the corners where R_i approaches zero. The corners therefore move the quickest towards the cube's center to reduce R_i, as illustrated in Fig. 8b. This movement causes areas close to the corner to bulge outward and eventually coalesce with neighboring domains. Quiescent phase inversion is thus inherently a corner phenomenon and it is expected that beyond a critical value, the distance between these corners, L, will have no effect on the time to phase inversion, t_c. This was confirmed in simulations using different values of $(h^* - h_c^*)$ and all further simulations were run where t_c^* was independent of $(h^* - h_c^*)$. In addition to reducing the parameter space, this substantially diminished the simulation's size.

The preceding discussion reduces $t_c^* = f(\rho_d/\rho_c, h^*, h_c^*, \lambda, Z)$ to $t_c^* = f(\lambda, Z)$. The viscosity ratio and Ohnesorge number could not a priori be eliminated from the analysis. As shown in Table 5, the computational viscosity-ratio range falls within the experimental one. However, the computational Ohnesorge number deviates from the experimental one by several orders of magnitude. This is because using the correct Ohnesorge number would have required trillions of time steps, which is infeasible even with the advanced computing resources available today.

In summary, the simulation models two Newtonian fluids in three dimensions where the interfacial-tension alone drives phase inversion. The minor-component concentration is sufficiently low that the time to phase inversion is independent of it. In the simulations, h and L were generally 4 or 6 and 46 or 66 lattice units, respectively, while h_c was two. The absolute viscosities varied between 0.03 and 0.1 mass/timestep lattice units and the surface tension between 0.02 and 0.2 mass/timestep^2 units.

Fig. 9 summarizes the simulation results for the viscosity-ratio range of 0.3–3.3. The data points indicate when the minor-component film first ruptured and phase inversion began. Regions below each point are at subcritical values of the dimensionless and dimensional times and have not yet phase inverted. Fig. 9 also shows the resulting master curve, which is the best line fit to the data. The lattice-Boltzmann simulations predict a functional dependence of the form $t_c^* \propto Z^{-0.36}\lambda_0^{-0.73}$ or $t_c \propto \eta_{minor}^{0.37}\eta_{major}^{0.27}$. Fig. 10 provides a comparison with the experimental data. The functional dependence determined by the lattice-Boltzmann simulation predicts quite well which blends have phase inverted. Note that the master curve was extrapolated beyond the simulation's viscosity-ratio and Ohnesorge-number range where it may be invalid. In addition, the absolute value of the master curve disagrees with the experimental data, as can be seen by comparing the vertical axes of Figs. 9 and 10. This may arise from the unrealistic sharpness of the corners in the model. In reality, the pellets have a finite radius of curvature which is expected to reduce the Laplace pressure driving the coalescence. A simulation testing this hypothesis indeed showed an increase in the time to phase inversion. Despite this shortcoming, however, the simulation qualitatively agrees very well with the experimental data. The dimensional form of the master curve predicts that the time to phase inversion t_c depends on $\eta_{minor}^{0.37}\eta_{major}^{0.27}$, the product of the viscosities rather than their ratio, just as was hypothesized earlier. This simultaneous

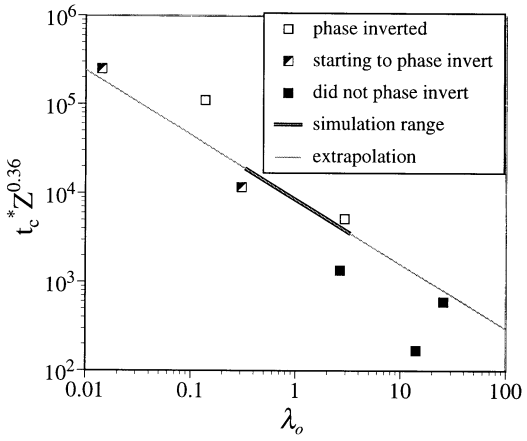

Fig. 10. Comparison of the experimental data with $t_c^* \propto Z^{-0.36}\lambda_0^{-0.73}$.

dependence on both component viscosities contrasts with Fortelny and Zivny's theory [14].

In summary, phase inversion was observed under quiescent conditions. The dependence of the time to phase inversion on the material properties was studied with lattice-Boltzmann simulations and dimensionless analysis. The resulting master curve shows a functional dependence of $t_c^* \propto Z^{-0.36}\lambda_0^{-0.73}$, which, when extrapolated to the experimental processing window, satisfactorily explained the experimental results. This master curve can potentially predict the time to phase inversion in situations that satisfy the model's assumptions. The dimensional time to phase inversion depended on the product of the component viscosities, unlike that of simple-shear flow, which depended on the viscosity ratio.

4. Conclusions

The effect of the components' rheologies on phase inversion was studied in both steady simple-shear flow and quiescent conditions. In the former flow field, the strain-dependent morphology development was determined. In the latter, samples were examined to determine if they had phase inverted after a set annealing time. In addition, the quiescent phase-inversion phenomenon was simulated using the lattice-Boltzmann method.

Blends subjected to steady, simple-shear flow went through qualitatively the same stages of morphology development, regardless of rheological properties. The results indicate that phase inversion initiates when the film separating the major-component domains locally thins to a critical value, 0.2–0.3 μm at low strain rates. Thus, the controlling parameter that dictates when phase inversion begins is the rate at which the film reaches this value. Under steady-simple-shear flow, the shear deformation controls film thinning. The effect of materials' properties on the rate of morphology development were compared with the literature with the concept of an effective viscosity ratio. Blends with lower effective viscosity ratios (major/blend) commenced phase inversion at lower strains. Once the major component had begun to coalesce, the rate of morphology development was described by the minor/blend viscosity ratio. The relevant phenomena here are drop deformation and capillary breakup. Breakup of the minor component proceeded more quickly as the effective viscosity ratio decreased. These results are consistent with most of the literature.

Under quiescent conditions, the driving force for film drainage is the Laplace pressure that pushes the deformed pellet toward a spherical shape. The lattice-Boltzmann simulations predict that the time to phase inversion depends on the product of the component viscosities rather than their ratio. The experimental results followed the functional dependence ($t_c^* \propto Z^{-0.36}\lambda_0^{-0.73}$ or $t_c \propto \eta_{minor}^{0.37}\eta_{major}^{0.27}$) of the simulation's master curve quite well, despite great differences between the experimental and computational Ohnesorge numbers and viscosity ratios. This functional dependence can potentially be used to predict the time to phase inversion under quiescent conditions for any blend where the rate of coalescence is controlled by the Laplace pressure. The pressure-driven film-drainage mechanism is expected to be active in simple-shear flow. It is a slow process, however and is easily overwhelmed by the shear deformation mechanism.

Acknowledgements

The authors thank Dr Alexander Wagner for fruitful discussions on the lattice-Boltzmann simulation. In addition, they gratefully acknowledge financial support from the National Science Foundation under Award Number DMI-9624388. Finally, this work made use of MRSEC Shared Facilities supported by the National Science Foundation under Award Number DMR-9400334.

Appendix A

The effective matrix viscosity was derived using the morphology shown in Fig. 6. The square repeat unit of this structure is a square major-component domain surrounded on all sides by minor-component films of equal thickness. If the repeat unit has a side of unit length, then the major component has a side of length $\sqrt{\phi_{major}}$. Therefore, the volume fraction of the B layer in Fig. 6, ϕ_B, is $\sqrt{\phi_{major}}$, and the volume fraction of the A layer, ϕ_A, is $1-\sqrt{\phi_{major}}$. The A layer is 100% minor component, while the B layer consists of $\sqrt{\phi_{major}}$ of the major component and $\left(1-\sqrt{\phi_{major}}\right)$ of the minor component. Using a series structure,

$$\eta_{eff} = \frac{\eta_A \eta_B}{\phi_A \eta_B + \phi_B \eta_A} \tag{A1}$$

where

$$\eta_A = \eta_{minor} \tag{A2}$$

$$\eta_B = \sqrt{\phi_{major}}\eta_{major} + \left(1 - \sqrt{\phi_{major}}\right)\eta_{minor} \tag{A3}$$

Substituting η_A, η_B, ϕ_A, ϕ_B, $\phi_1 = 1 - \sqrt{\phi_{major}}$, and $\phi_2 = \sqrt{\phi_{major}}$ into Eq. (A1) produces Eq. (1).

References

[1] Shih C-K. SPE ANTEC 1991;37:99–104.
[2] Ratnagiri R, Scott CE. Polym Engng Sci 1999;39(9):1823–35.
[3] Scott CE, Joung SK. Polym Engng Sci 1996;36(12):1666–74.
[4] Shih C-K. Adv Polym Technol 1992;11(3):223–6.
[5] Sundararaj U. Macromol Symp 1996;112:85–9.
[6] Sundararaj U, Macosko CW, Shih C-K. Polym Engng Sci 1996;36(13):1769–81.
[7] Lee JK, Han CD. Polymer 1999;40(23):6277–96.
[8] Lazo NDB, Scott CE. Polymer 1999;40(20):5469–78.
[9] Shih C-K. Polym Engng Sci 1995;35(21):1688–94.
[10] Ratnagiri R, Scott CE, Shih C-K. Polym Engng Sci 2001 (in press).
[11] Park I, Barlow JW, Paul DR. J Polym Sci B, Polym Phys 1992;30(9):1021–33.
[12] Scott CE, Macosko CW. Polym Engng Sci 1995;35(24):1938–48.
[13] Willemse RC, Ramaker EJJ, van Dam J, de Boer AP. Polym Engng Sci 1999;39(9):1717–25.
[14] Fortelny I, Zivny A. Polymer 1995;36(21):4113–8.
[15] Taylor GI. Proc R Soc A 1934;146:501–23.
[16] Grace HP. Chem Engng Commun 1982;14:225–77.
[17] Graebling D, Muller R, Palierne JF. Macromolecules 1993;26(2):320–9.
[18] Rumscheidt FD, Mason SG. J Colloid Sci 1961;16:238–61.
[19] Rallison JM. Annu Rev Fluid Mech 1984;16:45–66.
[20] Stone HA. Annu Rev Fluid Mech 1994;26:65–102.
[21] Marks CR. PhD thesis, University of Maryland, College Park, 1998.
[22] Zhao R, Macosko CW. SPE ANTEC 2000;46:1076–80.
[23] Elmendorp JJ, Van Der Vegt AK. Polym Engng Sci 1986;26(19):1332–8.
[24] Vrij A. Discuss Faraday Soc 1996;42:23–33.
[25] Grizzuti N, Bifulco O. Rheol Acta 1997;36(4):406–15.
[26] Tomotika S. Proc R Soc A 1935;150:322–37.
[27] Patlazhan SA, Lindt JT. J Rheol 1996;40(6):1095–113.
[28] Tjahjadi M, Ottino JM, Stone HA. AIChE J 1994;40(3):385–94.
[29] Smoluchowski M. Phys Z 1916;17:557.
[30] Smoluchowski M. Phys Z 1916;17:585.
[31] Smoluchowski M. Z Phys Chem 1917;92:129.
[32] Gunstensen AK, Rothman DH, Zaleski S, Zanetti G. Phys Rev A 1991;43(8):4320–7.
[33] Gunstensen AK, Rothman DH. Europhys Lett 1992;18:157–61.
[34] McNamara GR, Zanetti G. Phys Rev Lett 1988;61(20):2332–5.
[35] Van Genabeek O, Rothman DH. Annu Rev Earth Planet Sci 1996;24:63–87.
[36] Rothman DH, Zaleski S. Lattice-gas cellular automata: simple models of complex hydrodynamics. Cambridge, London: Cambridge University Press, 1997.
[37] Suwa ASM. Thesis, Massachusetts, Institute of Technology, Cambridge, 1998.
[38] Suwa A, Scott CE. SPE ANTEC 1998;44:232–6.
[39] Welty JR, Wicks CE, Wilson RE. Fundamentals of momentum. Heat, and mass transfer. New York: Wiley, 1976 (p. 154).